SIMPLE AND EFFICIENT NUMERICAL TOOLS FOR THE ANALYSIS OF PARACHUTES

Roberto Flores, Enrique Ortega and Eugenio Oñate

Centre Internacional de Mètodes Numèrics en Enginyeria (CIMNE)
Technical University of Catalonia (UPC)
08034 Barcelona, Spain
rflores@cimne.upc.edu; www.cimne.com

Abstract. This work describes a set of simple yet effective, numerical method for the design and evaluation of parachute-payload system. The developments include a coupled fluid-structural solver for unsteady simulations of ram-air type parachutes. For an efficient solution of the aerodynamic problem, an unsteady panel method has been chosen exploiting the fact that large areas of separated flow are not expected under nominal flight conditions of ram-air parachutes. A dynamic explicit finite element solver is used for the structure. This approach yields a robust solution even when highly non-linear effects due to large displacements and material response are present. The numerical results show considerable accuracy and robustness. An added benefit of the proposed aerodynamic and structural techniques is that they can be easily vectored and thus suitable for use in parallel architectures. The main features of the computational tools are described and several numerical examples are provided to illustrate the performance and capabilities of the technique.

1 INTRODUCTION

The numerical simulation of parachutes is a challenging problem as the geometry is complex in design and behaviour and, in addition, is continuously changing in time. Factors contributing to the complexity and unsteadiness of the aerodynamic field are massive flow separations, complex aerodynamic interactions between the structural components and the presence of large unsteady wakes. The structural analysis requirements are also challenging. Braced membranes, such as parachute canopies, cannot equilibrate an arbitrary set of loads unless drastic geometrical changes take place. The structural response is thus extremely nonlinear. In the case of follower loads (e.g. pressure loading) the matter is further complicated by the fact that the equilibrium solution may not exist at all (i.e. the structure is in fact a mechanism). This extreme geometrical nonlinearity can give rise to severe numerical convergence problems. Due to the lack of bending stiffness of the structural components, the materials are able to resist tensile stresses but buckle (wrinkle) under compressive loads [1,

1

2]. This asymmetric behaviour should also be accounted for. Finally, the nature of the applied forces which depend heavily on the structural response of the parachute adds an extra layer of complexity to the analysis. As the magnitude and direction of the aerodynamic forces are not known in advance but are a function of the deformed parachute shape, they must be computed as part of the solution in an iterative process. A comprehensive review of the topic of parachute simulation can be found in [20].

An effective numerical model of parachutes must deal with all the issues listed above in a robust way while keeping computational cost at an acceptable level. The magnitude of the challenges faced explains why the current design of parachute systems relies mostly on empirical methods. From the point of view of a parachute designer two features of outmost importance are the in-flight shape (which guides the rigging design, i.e. the distribution of suspension lines) and the stresses on the fabric and cables. Unfortunately current industrial practice calls for a multitude of prototypes to be built in order to find a suitable configuration. The process relies heavily on the intuition of the designer and is lengthy as well as costly. Matters are further complicated by the inherent difficulty of instrumenting the canopy. Standard strain gages are not well suited to the task as their mechanical properties are not a good match to the fabric (i.e. they interfere with the behaviour of the canopy). Experimental measurements are thus scarce and unreliable.

As an example, 15 worldwide parachute manufacturers were recently surveyed about the use of computational tools in the design and evaluation of parachute systems [3]. None of those 10 who provided feedback declared using computer tools beyond CAD packages for geometry modelling. This is a clear indication that computational mechanics does not yet enjoy wide acceptance among the parachute design industry. The numerical simulation tool described in this work is intended to address the needs of this sector.

In the following, the main features of the parachute simulation tool developed by the authors are described and several numerical applications are presented with the aim of illustrating the performance and potential of the proposed techniques. The rest of the document is organized into 4 main sections. The core features of the coupled fluid-structural solver are given in section 2. Next, validation cases for the structural and flow solvers are presented in section 3 and numerical applications are shown in section 4. Finally, the main conclusions are summarized in section 5.

2. COUPLED SOLUTION STRATEGY

In view of the important challenges involved in modelling parachute systems, the choice of the structural and aerodynamic solvers as well as the coupling methodology were thoroughly examined from two different points of view. First, considering the capabilities of the techniques to deal with the typical situations encountered during the flight of parachutes; second, evaluating its robustness and the chances of achieving low computational costs through efficient numerical implementations.

Regarding structural modelling, it was decided to use a FE dynamic structural solver. An unsteady analysis is not affected by problems caused by the lack of a definite static equilibrium configuration. In fact, since for dynamic problems the structure is constantly in equilibrium with the inertial forces the solution is always unique. Even when only the long-term static response is sought, the dynamic approach offers some advantages. Furthermore, the extension to transient dynamic problems becomes trivial.

There are two basic kinds of dynamic solvers, implicit and explicit [4]. Implicit solvers can be made unconditionally stable, which allows for large time steps although the computational cost is high because a non-linear problem must be solved at each time step. When the structural response does not show a high deviation from linearity the implicit treatment is usually preferred, as it allows for large time steps. Also, the static equilibrium (when it exists) can be reached after a small number of iterations. However, it should be stressed that the radius of convergence of the iterative algorithms employed for solving the non-linear system is limited. Thus, the time step cannot be made arbitrarily large. In addition, when the structural behaviour is heavily non-linear, the time increment must be cut back to ensure convergence of the iterative algorithm and the computational cost is rapidly increased. Implicit solvers also exhibit a lack of robustness due to the possibility of the scheme failing to converge. On the other hand, although the explicit solvers are conditionally stable (the stability limit is determined by the material properties and the geometry of the FE mesh) the cost per time step is low. The explicit method is extremely insensitive to highly nonlinear structural behaviour and requires a number of time steps that does not change substantially as the system response becomes more complex. Material nonlinearities and large displacements, which are extremely detrimental for the convergence behaviour of the implicit scheme, do not affect adversely the explicit algorithm. In view of the difficulties expected, the choice was made to use an explicit FE structural solver. A further benefit is the ability of the algorithm to be easily vectored and thus take advantage of modern parallel processing architectures. Linear

cable and membrane elements were selected due to their ease of implementation. The fabric is modelled using three-node membrane elements due to their geometric simplicity. The three nodes of the element will always lie in the same plane so the definition of the local coordinate systems is straightforward. A local co-rotational reference frame is used for each cable and membrane element in order to remove the rigid-body displacements and isolate the material strains. Inside each element a simple small-strain formulation is used due to the properties of the fabric. Tensile deformations are always small; on the other hand compressive strains can become extremely large due to the inclusion of a wrinkling model (zero compression stiffness). There is, however, no stress associated with the compressive strains and, correspondingly, no strain energy. Therefore, the small-strain formulation is adequate as only tensile deformations must be taken into account to calculate the stress state.

In spite of the fact that the structural solution approach is general and can be applied to any kind of parachute system, the computational cost of a general flow solution was not feasible from a practical point of view (at least during the first stages of the work) and a decision had to be taken regarding the scope of the aerodynamic solution. Consequently, following previous in-house developments, the focus was initially placed on ram-air type parachutes for which a potential flow approach is valid as no extensive separation regions are present during nominal operation. The main advantage of the potential model is that boundary methods can be employed. Hence, most problems related to grid generation can be avoided. Due to the large geometric changes expected, methods based on discretization of the surrounding air volume would need multiple remeshing steps. For the boundary mesh, however, only changes to the nodal position are required as the topology remains unchanged. As an added benefit, the computational cost is significantly reduced with respect to volume techniques (e.g. Finite Differences, Finite Volumes and Finite Elements). In order to obtain a reasonable approximation of the deformed canopy geometry and stress field the pressure field from the inviscid solution is usually appropriate. The potential approach can therefore provide valuable data for the parachute designer. Even in cases when extensive flow separation occurs, alternative potential approaches such as vortex methods could be used. In other cases, for problems going beyond the scope of potential methods, the modular approach adopted for the code allows changing the flow solver with minimal modifications.

2.1 The structural model

This starting point for solving the structural problem is the virtual work principle. It states that when the system is in equilibrium the change in strain energy caused by an arbitrary virtual displacement field equals the work done by the external forces.

$$\sum_{i,j} \int_\Omega \sigma_{ij} \delta\varepsilon_{ij}\, d\Omega = \sum_i \int_\Omega b_i \delta u_i\, d\Omega + \sum_i \int_{\Gamma_N} \overline{t_i} \delta u_i\, d\Gamma \tag{1}$$

where $\overline{t_i}$ stands for prescribed surface traction on the boundary Γ_N. σ_{ij} denotes the components of the stress tensor and $\delta\varepsilon_{ij}$ is the virtual strain corresponding to the virtual displacement field δu_i. In the case of a dynamic problem the body forces (b_i) must include the inertial loads given by

$$b_i\big|_{inertial} = -\rho \frac{d^2 u_i}{dt^2} \tag{2}$$

In (2) ρ is the density of the solid. Note that a total derivative (i.e. tracking the material particles) is used. The complete set of boundary conditions is:

$$\sum_j \sigma_{ij} \cdot n_j = \overline{t_i}(\mathbf{x}) \quad \forall\, \mathbf{x} \in \Gamma_N$$
$$u_i = \overline{u_i}(\mathbf{x}) \quad \forall\, \mathbf{x} \in \Gamma_D \tag{3}$$

with $\overline{u_i}$ being the prescribed displacements on the boundary Γ_D. It is assumed that the virtual displacements in (1) vanish over the surface Γ_D.

2.1.1 Finite element discretization

In order to obtain a discretized form of the governing equation (1) an approximate FE solution is build by interpolating the nodal values of the displacements [5]. In a similar manner, a virtual displacement field can be obtained, thus

$$\tilde{u}_i(\mathbf{x}) = N^k(\mathbf{x})\tilde{u}_i^k \quad \delta u_i(\mathbf{x}) = N^k(\mathbf{x})\delta u_i^k \tag{4}$$

$\tilde{u}_i$ being the approximate solution and N^k the interpolation (shape) function corresponding to the kth node of an element (from now on supra-indexes will indicate nodal values). In (4) summation is assumed over the repeated index (k). The sum extends from 1 to n_{nod} (the total number of nodes in the mesh). As the virtual strain field is a linear function of the virtual displacement field, it is also a linear function of δu_i^k. Therefore, it is possible to write

$$\delta\varepsilon_{ij} = A_{ij,m}^{k}\delta u_{m}^{k} \qquad A_{ij,m}^{k} = \frac{\partial\varepsilon_{ij}}{\partial u_{m}^{k}} = L(N^{k}) \tag{5}$$

Introducing the interpolated solution into (1) and taking into account that the virtual nodal displacements are arbitrary the following discretized form is obtained (note that the inertial loads have been included)

$$\int_{\Omega}\rho N^{b}N^{k}d\Omega\frac{d^{2}u_{a}^{k}}{dt^{2}} = \int_{\Omega}b_{a}N^{b}d\Omega + \int_{\Gamma_{N}}\overline{t}_{a}N^{b}d\Gamma - \int_{\Omega}\sigma_{kj}A_{kj,a}^{b}d\Omega \tag{6}$$

where $a = 1,2,3$, $b = 1,...,n_{nod}$ and summation is assumed over the j and k indices. These equations can also be written in matrix form as

$$\mathbf{M\ddot{u}} = \mathbf{b} + \mathbf{t} - \mathbf{I} \tag{7}$$

$\mathbf{M}$ is the mass matrix of the system, $\mathbf{b}$ and $\mathbf{t}$ represent the external nodal generalized forces and $\mathbf{I}$ is the internal force vector. The system of ordinary differential equations given by Eq. (7) along with suitable initial conditions

$$\begin{aligned}\mathbf{u}\big|_{t=o} &= \mathbf{u_0}\\ \dot{\mathbf{u}}\big|_{t=o} &= \dot{\mathbf{u}}_{\mathbf{0}}\end{aligned} \tag{8}$$

can be advanced in time to yield the displacement field at every instant time. To speed up the computations without significant loss of accuracy, the mass matrix $\mathbf{M}$ is usually replaced by its lumped (diagonal) counterpart given by

$$M_{ij}^{d} = \delta_{ij}\sum_{j}M_{ij} \tag{9}$$

where δ_{ij} denotes Kronecker's delta function. In order to build the terms appearing in Eq. (7) an element-by-element approach is adopted. As the shape function of node k is nonzero only inside elements containing it, the integrals need only evaluated in the appropriate elements, e.g.

$$M_{ij} = \int_{\Omega}\rho N^{i}N^{j}d\Omega = \sum_{el}\int_{\Omega_{el}}\rho N^{i}N^{j}d\Omega \quad / \ i,j \subset el \tag{10}$$

2.1.2 Time integration

The system of equations (7) is advanced explicitly in time by means of a second order central differencing scheme, selected due to its high efficiency and acceptable accuracy [4]. Thus, given a series of points in time and their corresponding time increments

6

$$t^{(0)} \ , \ ... \ , \ t^{(i-1)} \ , \ t^{(i)} \ , \ t^{(i+1)} \ , \ ...$$
$$... \ , \ \Delta t^{(i)} = t^{(i)} - t^{(i-1)} \ , \ \Delta t^{(i+1)} = t^{(i+1)} - t^{(i)} \ , \ ...$$

(11)

the change in midpoint velocity can be defined as

$$\frac{d\mathbf{u}^{\left(i+\frac{1}{2}\right)}}{dt} - \frac{d\mathbf{u}^{\left(i-\frac{1}{2}\right)}}{dt} = \frac{\Delta t^{(i+1)} + \Delta t^{(i)}}{2} \cdot \frac{d^2\mathbf{u}^{(i)}}{dt^2}$$

(12)

where the accelerations and velocities are evaluated at different instants times. This scheme provides second order accuracy in time by virtue of the centered approximation for the time derivative. Once the intermediate velocities have been computed, the displacements can be updated using

$$\mathbf{u}^{(i+1)} = \mathbf{u}^{(i)} + \Delta t^{(i+1)} \cdot \frac{d\mathbf{u}^{\left(i+\frac{1}{2}\right)}}{dt} = \mathbf{u}^{(i)} + \Delta t^{(i+1)} \cdot \left[\frac{d\mathbf{u}^{\left(i-\frac{1}{2}\right)}}{dt} + \frac{\Delta t^{(i+1)} + \Delta t^{(i)}}{2} \cdot \frac{d^2\mathbf{u}^{(i)}}{dt^2} \right]$$

(13)

The method outlined has an extremely low computational cost per time step; however, it shows a very important limitation. The explicit scheme is only conditionally stable meaning the time increment must be limited in order to prevent divergence of the solution. The maximum allowable time step is given by

$$\Delta t \le \frac{2}{\omega_{max}}$$

(14)

with ω_{max} being the angular frequency of the highest eigenmode of the system. An alternative estimate of the maximum time step is given by the minimum transit time of the dilatational waves across the elements of the mesh, i.e.

$$\Delta t \le \min\left(\frac{L_e}{c_d} \right)$$

(15)

where L_e is a characteristic element dimension and c_d is the dilatational wave speed. For an isotropic linear elastic solid the speed of sound is

$$c_d = \sqrt{\frac{\lambda + 2\mu}{\rho}}$$
$$\lambda = K - \frac{2}{3}G \ \ ; \ \ \mu = G = \frac{E}{2(1+\nu)} \ \ ; \ \ K = \frac{E}{3(1-2\nu)}$$

(16)

where λ and μ are the Lamé constants which can be calculated from the shear modulus (G) and bulk modulus (K) of the material as stated above. Alternatively, it is possible to use

Young's modulus (E) and Poissons ratio (ν) as independent material parameters as indicated in (16).

2.1.3 Numerical damping

In order to achieve a smooth solution of the problem, some numerical damping must be introduced in the equations. Two forms of user-adjustable damping are included to improve control over the solution process: Rayleigh damping and bulk viscosity. In the first case the damping matrix is built from the mass and stiffness matrices

$$\mathbf{C} = \alpha\mathbf{M} + \beta\mathbf{K} \tag{17}$$

Hence, the equation system (7) supplemented with this damping term becomes

$$\mathbf{M}\ddot{\mathbf{u}} = \mathbf{b} + \mathbf{t} - \mathbf{I} - \mathbf{C}\dot{\mathbf{u}} \tag{18}$$

The α term creates a damping force proportional to the absolute velocity of the nodes which is called mass proportional damping. This is roughly equivalent to having the nodes of the structure move through a viscous fluid. The damping ratio introduced by the mass proportional damping term on a mode of frequency ω is

$$\xi = \frac{\alpha}{2\omega} \tag{19}$$

From Eq. (19) it is apparent that the α term affects mainly the low frequency components of the solution. Thus, it can be useful to accelerate convergence to a static solution when only the long-term response is sought. On the other hand, the β term introduces forces that are proportional to the material strain rate (this kind of dissipation is termed "stiffness proportional damping"). An extra stress $\boldsymbol{\sigma_d}$ is added to the constitutive law

$$\boldsymbol{\sigma_d} = \beta\mathbf{D}^{el} : \dot{\boldsymbol{\varepsilon}} \tag{20}$$

with $\mathbf{D}^{el}$ being the tangent stiffness tensor of the material. The fraction of critical damping for a given mode is

$$\xi = \frac{\beta\,\omega}{2} \tag{21}$$

In this case only the high order modes are affected appreciably. An additional form of damping is included to prevent high frequency "ringing". This is caused by excitation of element dilatational modes which are always associated with the highest eigenvalues of the

system. An additional hydrostatic stress is included in the constitutive routines which is proportional to the volumetric strain rate. This volumetric viscous stress is given by

$$\sigma_h = b\,\rho\,c_d\,L_e\,\dot{\varepsilon}_{vol} \tag{22}$$

where b is the desired damping ratio for the dilatational mode.

2.1.4 Element formulation

Linear two-node cables and three node membranes are employed. As an introduction to the details of implementation, the cable element formulation is described first. While extremely simple, it contains many of the relevant features needed to formulate the surface element. As only small tensile strains are expected, a small-strain formulation has been adopted to calculate the elemental stresses. This assumption allows for efficient coding while maintaining acceptable accuracy.

2.1.4.1 Two-node linear cable element

Let us consider a linear cable element stretching between nodes i and j, having cross sectional area A and subject to a distributed loading per unit length $\mathbf{f_d}$ as shown in Fig. 1.
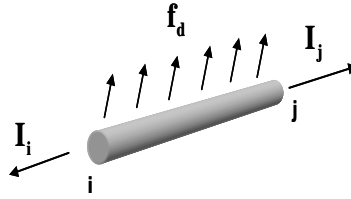
Figure 1. Linear cable element subject to internal and external loads.

As large displacements are expected, the position of the nodes can be written either on the undeformed (reference) configuration or in the deformed (current) configuration. From now on upper-case letters will denote the original coordinates while lower-case will be reserved for the current configuration. For example, the original length of the cable element is given by

$$L_0 = \left\| \mathbf{X_j} - \mathbf{X}_i \right\| \tag{23}$$

while the actual length at any given time is

$$L(t) = \left\| \mathbf{x_j} - \mathbf{x_i} \right\| \tag{24}$$

The unit vector along the element is

$$\mathbf{e_l} = \frac{\mathbf{x_j} - \mathbf{x_i}}{\left\| \mathbf{x_j} - \mathbf{x_i} \right\|} \tag{25}$$

From the change in length of the element the axial strain and stress can be obtained. Assuming linear elastic behaviour

$$\varepsilon = \frac{L - L_0}{L_0} \quad ; \quad \sigma = \max(0, E\varepsilon) \tag{26}$$

The cables buckle instantly under compressive loads, thus, there is a lower bound of zero is enforced in Eq. (26). The internal forces acting at the nodes are

$$\mathbf{I_i} = -\sigma A \mathbf{e_l} \quad ; \quad \mathbf{I_j} = +\sigma A \mathbf{e_l} \tag{27}$$

Note that in (27) no distinction has been made between the reference (A_0) and the updated cross-section (A). When the element is active (under tension) the strains are always small so either value is acceptable. The nodal generalized external force due to the distributed loading is calculated as indicated in Eq. (6). If the load $\mathbf{f_d}$ is constant across the element it reduces to

$$\mathbf{b_i} = \int_0^L N_i \mathbf{f_d} dL = \frac{L}{2} \mathbf{f_d} \tag{28}$$

When numerical damping is included the stress term in Eq. (26) is augmented with the viscous contributions

$$\frac{d\varepsilon}{dt} = \frac{(\dot{\mathbf{x}}_j - \dot{\mathbf{x}}_i) \cdot \mathbf{e_l}}{L_0} \quad ; \quad \sigma = E\left(\max(0, \varepsilon) + \beta\dot{\varepsilon}\right) + b\,\rho\,c_d\,L_0\,\dot{\varepsilon} \tag{29}$$

The elemental mass matrix can be obtained using Eq. (10)

$$\mathbf{M} = \rho AL \begin{bmatrix} \frac{1}{3} & \frac{1}{6} \\ \frac{1}{6} & \frac{1}{3} \end{bmatrix} \quad ; \quad \mathbf{M^d} = \frac{\rho AL}{2} \begin{bmatrix} 1 & 0 \\ 0 & 1 \end{bmatrix} \tag{30}$$

In many occasions the CAD geometry available does not reflect the nominal (i.e. in-flight) length of the suspension lines. In particular, this is quite common for the brake lines which the pilot must pull once the canopy is deployed. During manoeuvres further changes to the cable lengths must be enforced in order to obtain the correct response. The control demands can be reproduced either using a combination of sliding cable elements and prescribed displacements or, in a much more simple way, by changing the undeformed cable length. To this effect, the code allows the user to change the L_0 value in (29) as the simulation progresses. The time evolution of L_0 for the relevant elements can be specified as part of the input file.

2.1.4.2 Three-node linear membrane element

A triangular element with three corner nodes $\mathbf{x}^1$, $\mathbf{x}^2$ and $\mathbf{x}^3$ is defined according to figure 2. Given that large displacements are expected, the strain state of the element is easier to evaluate in a local corrotational frame than in the global reference system [6].
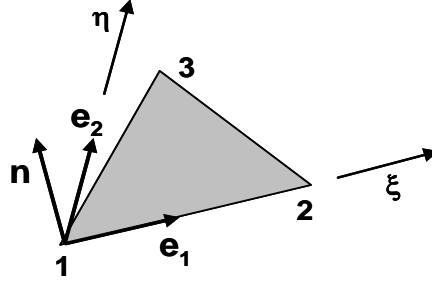

Figure 2. Linear membrane element corrotational local frame.

The three unit vectors along the local axes are obtained from

$$\mathbf{e}_1 = \frac{\mathbf{x}^2 - \mathbf{x}^1}{\left\| \mathbf{x}^2 - \mathbf{x}^1 \right\|} \quad ; \quad \mathbf{n} = \frac{\mathbf{e}_1 \times (\mathbf{x}^3 - \mathbf{x}^1)}{\left\| \mathbf{e}_1 \times (\mathbf{x}^3 - \mathbf{x}^1) \right\|} \quad ; \quad \mathbf{e}_2 = \mathbf{n} \times \mathbf{e}_1 \tag{31}$$

Thus, any point of the triangle can now be identified by its two local coordinates (ξ, η) by

$$(\xi, \eta) = \left((\mathbf{x} - \mathbf{x}^1) \cdot \mathbf{e}_1, (\mathbf{x} - \mathbf{x}^1) \cdot \mathbf{e}_2 \right) \tag{32}$$

As a linear triangle always remains flat, the problem is greatly simplified by analysing the stress state on the ξ-η plane.
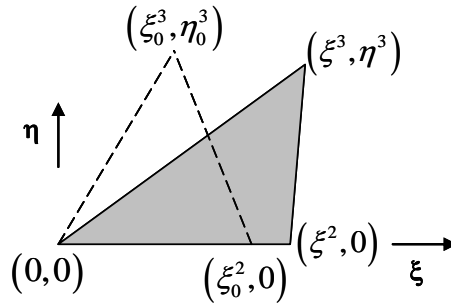
Figure 3. Nodal coordinates in the triangle local reference frame.

The components of the strain tensor can be determined easily using the gradients of the element shape functions

$$
\begin{bmatrix} \varepsilon_\xi \\ \varepsilon_\eta \\ \gamma_{\xi\eta} \end{bmatrix} = \begin{bmatrix} \dfrac{\partial N^1}{\partial \xi} & 0 & \dfrac{\partial N^2}{\partial \xi} & 0 & 0 & 0 \\[2mm] 0 & \dfrac{\partial N^1}{\partial \eta} & 0 & \dfrac{\partial N^2}{\partial \eta} & 0 & \dfrac{\partial N^3}{\partial \eta} \\[2mm] \dfrac{\partial N^1}{\partial \eta} & \dfrac{\partial N^1}{\partial \xi} & \dfrac{\partial N^2}{\partial \eta} & \dfrac{\partial N^2}{\partial \xi} & \dfrac{\partial N^3}{\partial \eta} & 0 \end{bmatrix} \begin{bmatrix} u_\xi^1 \\ u_\eta^1 \\ u_\xi^2 \\ u_\eta^2 \\ u_\xi^3 \\ u_\eta^3 \end{bmatrix}
\tag{33}
$$

Note that several of the displacements are zero (i.e. $u_\xi^1 = u_\eta^1 = u_\eta^2 = 0$) by virtue of the definition of the coordinate system. However Eq. (33) is still useful because it can be used with an arbitrary virtual displacement field. The shape function gradients in the equation are computed from an isoparametric transform [5]. The corresponding stresses are calculated assuming a plane stress state (an acceptable hypothesis for thin surface elements) and linear elastic isotropic behaviour. Hence,

$$
\begin{bmatrix} \sigma_\xi \\ \sigma_\eta \\ \tau_{\xi\eta} \end{bmatrix} = \frac{E}{1-\nu^2} \begin{bmatrix} \varepsilon_\xi + \nu \varepsilon_\eta \\ \varepsilon_\eta + \nu \varepsilon_\xi \\ \dfrac{1-\nu}{2} \gamma_{\xi\eta} \end{bmatrix}
\tag{34}
$$

As the membrane buckles under compressive loads, the stresses given by Eq. (34) must be corrected to account for this fact [7]. To this end we shall refer to Eq. (34) as the trial stress state σ^t. Then, three possible membrane states, depicted in Figure 4, are considered:

- Taut: the minimum principal trial stress is positive. No corrections are needed.
- Wrinkled: membrane is not taut, but the maximum principal strain is positive. Trial state is replaced with a uniaxial stress state.
- Slack: the maximum principal strain is negative. The corrected stresses are zero.
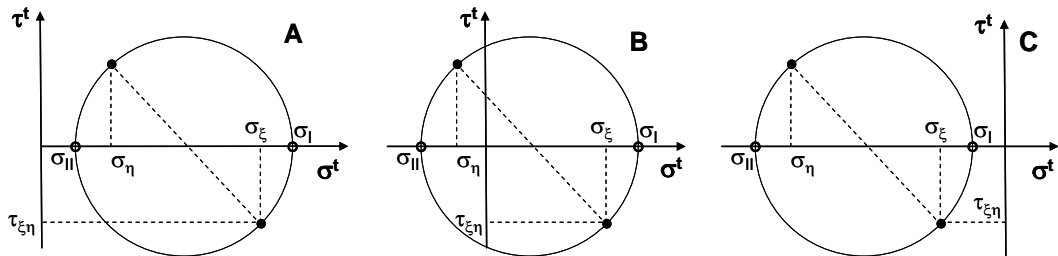

Figure 4. Trial membrane states: taut (A), wrinkled (B) and slack (C).

When the membrane is wrinkled the stress state must be corrected (see Figure 5). First, the average in-plane direct strain, maximum shear strain and maximum principal strain are obtained from

$$\varepsilon_m = \frac{\varepsilon_\xi + \varepsilon_\eta}{2} \;\; ; \;\; \frac{\gamma_{max}}{2} = \sqrt{\left(\frac{\varepsilon_\xi - \varepsilon_\eta}{2}\right)^2 + \frac{\gamma_{\xi\eta}^2}{4}} \;\; ; \;\; \varepsilon_I = \varepsilon_m + \frac{\gamma_{max}}{2} \tag{35}$$

Using the values in (35) the stress state is corrected in the principal strain directions and then rotated back to the ξ-η axes

$$\sigma_I = E\varepsilon_I \;\; ; \;\; \sigma_{II} = 0 \;\; ; \;\; \sigma_m = \frac{\sigma_I}{2}$$

$$\sigma_\xi = \sigma_m\left(1 + \frac{\varepsilon_\xi - \varepsilon_\eta}{\gamma_{max}}\right) \;\; ; \;\; \sigma_\eta = \sigma_m\left(1 - \frac{\varepsilon_\xi - \varepsilon_\eta}{\gamma_{max}}\right) \;\; ; \;\; \tau_{\xi\eta} = \sigma_m \frac{\gamma_{\xi\eta}}{\gamma_{max}} \tag{36}$$
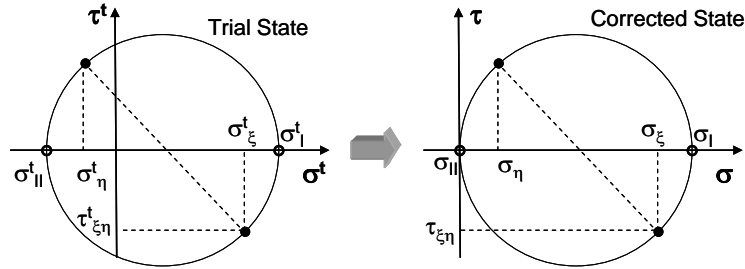
Figure 5. Stress correction for wrinkled membrane.

The elastic stresses are next augmented with viscous terms to introduce a suitable level of numerical damping. Using the nodal velocities the components of the strain rate tensor can be computed. The damping stresses are then given by

$$\begin{bmatrix} \sigma_\xi \\ \sigma_\eta \\ \tau_{\xi\eta} \end{bmatrix}_{damp} = \frac{\beta E}{1-\nu^2} \begin{bmatrix} \dot{\varepsilon}_\xi + \nu\dot{\varepsilon}_\eta \\ \dot{\varepsilon}_\eta + \nu\dot{\varepsilon}_\xi \\ \frac{1-\nu}{2}\dot{\gamma}_{\xi\eta} \end{bmatrix} + b\rho c_d L\left(\dot{\varepsilon}_\xi + \dot{\varepsilon}_\eta\right) \begin{bmatrix} 1 \\ 1 \\ 0 \end{bmatrix} \tag{37}$$

The total stress (elastic plus viscous) is then used to calculate the nodal forces evaluating the change in strain energy due to a virtual displacement of the nodes. As the triangular linear elements create a constant strain (and stress) field a single point Gauss quadrature is adequate

$$\int \boldsymbol{\sigma} : \delta\boldsymbol{\varepsilon} \, d\Omega = tA_0\left(\sigma_\xi \delta\varepsilon_\xi + \sigma_\eta \delta\varepsilon_\eta + \tau_{\xi\eta} \delta\gamma_{\xi\eta}\right) \tag{38}$$

with t being the element thickness and A_0 its reference (undeformed) area.

When the element faces are subject to a pressure loading, the corresponding nodal generalized forces are obtained from Eq. (6). For the particular case of a uniform pressure p acting on the upper side of the element (the side towards which the normal vector $\mathbf{n}$ points) the nodal forces are

$$\begin{bmatrix} I_n^1 \\ I_n^2 \\ I_n^3 \end{bmatrix} = -\frac{pA_p}{3} \begin{bmatrix} 1 \\ 1 \\ 1 \end{bmatrix} \tag{39}$$

where A_p stands for current projected area of the element. Finally, once all the components of the internal forces have been determined on the local reference frame, the global force vector can be assembled. The transformation to the global inertial reference system is performed through

$$\mathbf{I_{glob}^i} = I_\xi^i \mathbf{e_1} + I_\eta^i \mathbf{e_2} + I_n^i \mathbf{n} \tag{40}$$

Finally, assuming uniform density, the mass matrices for the element are given by

$$\mathbf{M} = \frac{\rho t A_0}{3} \begin{bmatrix} \frac{1}{2} & \frac{1}{4} & \frac{1}{4} \\ \frac{1}{4} & \frac{1}{2} & \frac{1}{4} \\ \frac{1}{4} & \frac{1}{4} & \frac{1}{2} \end{bmatrix} \; ; \; \mathbf{M^d} = \frac{\rho t A_0}{3} \begin{bmatrix} 1 & 0 & 0 \\ 0 & 1 & 0 \\ 0 & 0 & 1 \end{bmatrix} \tag{41}$$

2.2 The aerodynamic model

An unsteady low-order panel method is adopted in this work under the assumption that a potential flow approach is valid for normal flight conditions of ram-air parachutes. The problem setup consists of an arbitrary body (parachute-payload system) immerse in an ideal fluid filling a domain Ω inside the far-field boundary S_∞. The body is defined by boundary S_B and S_W represents the upper (U) and lower (L) sides of a thin wake extending downstream from the body. The boundaries $S_B + S_W$ divide the problem domain into external and internal regions having harmonic potentials Φ and Φ_i respectively.
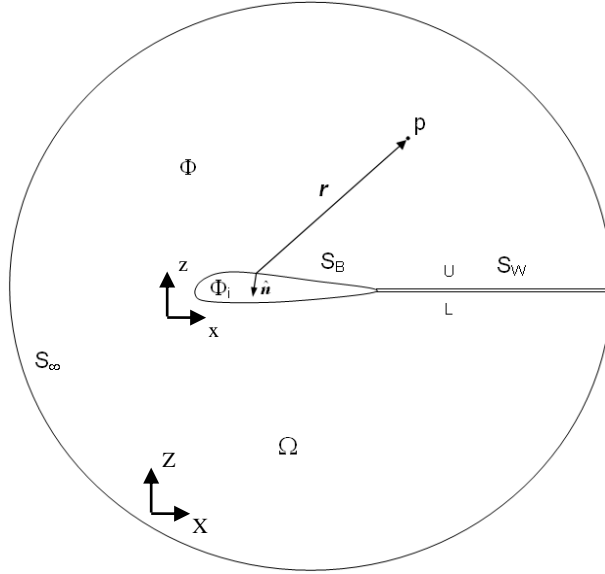
Figure 6. Aerodynamic problem setup.

To simplify the treatment of unsteady problems, a body-fixed coordinate system (x,y,z) and an inertial reference frame (X,Y,Z) are defined. The body system is attached to the solid and follows its motion. At time $t = 0$ both coordinates systems are coincident with no relative motion; at time $t > 0$, the position and orientation of the body system is determined from the flight path data.

In order to solve the problem described above, a general solution for the velocity potential at any point p can be obtained by applying Green's theorem [8]. This leads to

$$\Phi_p = \frac{1}{4\pi} \iint_{S_B} \mu \nabla\left(\frac{1}{r}\right) \cdot \hat{\boldsymbol{n}} \, dS - \frac{1}{4\pi} \iint_{S_B} \left(\frac{\sigma}{r}\right) dS + \frac{1}{4\pi} \iint_{S_W} \mu_W \nabla\left(\frac{1}{r}\right) \cdot \hat{\boldsymbol{n}} \, dS + \phi_\infty(\mathrm{p}) \qquad (42)$$

where r is the distance between the point p and a surface element dS having normal vector $\hat{\boldsymbol{n}}$ pointing outside Ω, ϕ_∞ is a constant freestream potential due to S∞ and no jump in the normal component of the velocity across the wake is considered (thin wake assumption). The terms $-\mu = \Phi - \Phi_i$ and $-\sigma = \nabla(\Phi - \Phi_i) \cdot \hat{\boldsymbol{n}}$ represent the strength (per unit area) of doublet and source surface distributions which account for, respectively, jumps in potential and in the normal velocity component across the boundaries. In order to solve Eq. (42), the internal Dirichlet condition $\Phi_i = const. = \phi_\infty$ is applied. The velocity potential can be split into a freestream potential ϕ_∞ plus a perturbation potential due to the body and its wake $\phi = \Phi - \phi_\infty$. For a point p inside the body Eq. (42) becomes

$$0 = \frac{1}{4\pi} \iint_{S_B} \mu \nabla \left(\frac{1}{r} \right) \cdot \hat{\boldsymbol{n}} \, dS - \frac{1}{4\pi} \iint_{S_B} \left(\frac{\sigma}{r} \right) dS + \frac{1}{4\pi} \iint_{S_W} \mu_W \nabla \left(\frac{1}{r} \right) \cdot \hat{\boldsymbol{n}} \, dS \tag{43}$$

where the doublet strength turns into the perturbation velocity potential $-\mu = \phi = \Phi - \phi_\infty$ and the source strength is $-\sigma = \nabla(\Phi - \phi_\infty) \cdot \hat{\boldsymbol{n}}$. At this point some assumptions must be done to solve Eq. (43); the first one is related to the source distribution. Assuming that the normal velocity across the body boundaries is zero (slip condition) or some known value (transpiration), the source strengths σ can be determined through Neumann boundary conditions [8]. This leads to

$$\sigma = -\mathbf{V}_T - \mathbf{v} \cdot \hat{\boldsymbol{n}} = -\mathbf{V}_T - \left(\mathbf{V}_0 + \boldsymbol{\omega} \times \boldsymbol{r} + \mathbf{v}_{rel} \right) \cdot \hat{\boldsymbol{n}} \tag{44}$$

where $\mathbf{v}$ is the instantaneous kinematic velocity (due to the velocity of the body system's origin $\mathbf{V}_0$, the spin rate $\boldsymbol{\omega}$ of the solid and relative velocities $\mathbf{v}_{rel}$ due to deformations in the body's frame). $\mathbf{V}_T$ is a specified normal velocity relative to the boundary (transpiration velocity) which is zero when the boundaries are airtight. The second assumption allows writing the wake doublicity μ_W in terms of the body doublets by means of the Kutta condition [8]. This empirical-base condition, which enforces zero resultant vorticity along shedding lines, allows the flow to separate smoothly at body trailing edges and fixes the correct amount of circulation for lifting problems. Once the source and wake doublet distributions have been determined, it is possible to solve Eqs. (43) for the unknown body doublicity. To this end, a discrete form of the governing equations (43) is obtained by breaking down the surface integrals into integrals over quadrilateral and/or triangular flat panels distributed along the body and the wake, *cf.* [8, 9] for details. The discrete equation system is solved iteratively by means of a bi-conjugate gradient solver. Note that the kinematic velocity changes in time as a consequence of the body motion and this introduces time dependence in the potential problem solution given by Eq. (43).

2.2.1 Wake treatment

The wake extending from the body is modeled by means of a time-steeping technique [10]. In this way, the wake develops according to the motion of the body during a time-marching simulation. As mentioned before, the wake doublicity of the panels shed into the wake is determined by enforcing the Kutta condition at the shedding lines. Due to the conservation of vorticity, the doublicity of the fluid particles forming the wake must not change. Therefore,

the wake strength is convected downstream. In addition, at the end of each time step a wake rollup procedure [8] is performed to align the wake panels with the local flow streamlines.

2.2.2 Computation of loads

The aerodynamic loads acting on the body are computed by means of the unsteady form of Bernoulli's equation. Thus, the coefficient of pressure (Cp) can be calculated at any point as

$$Cp = \frac{p - p_\infty}{\frac{1}{2}\rho_\infty V_\infty^2} = 1 - \left(\frac{V}{V_\infty}\right)^2 - \frac{2}{V_\infty^2}\frac{\partial \phi}{\partial t} \tag{45}$$

being V the magnitude of the total velocity at the control point (kinematic + perturbation) and V_∞ the magnitude of the reference freestream velocity. The unsteady term can be computed as $\partial \phi / \partial t = -\partial \mu / \partial t = -(\mu_t - \mu_{t-\Delta t})/\Delta t$. The tangential components of the perturbation velocity are evaluated by taking the gradient of μ in panel coordinates. Hence,

$$q_l = \frac{\partial \mu}{\partial \hat{l}} \quad , \quad q_m = \frac{\partial \mu}{\partial \hat{m}} \tag{46}$$

and the normal component of the velocity is given by

$$q_n = \sigma \tag{47}$$

being σ the panel's source strength (44). Then, the total velocity on a given panel is obtained by adding the perturbation velocity to the instantaneous local kinematic velocity, i.e.

$$\mathbf{V} = q_l * \hat{l} + q_m * \hat{m} + q_n * \hat{n} + \left(\mathbf{V}_0 + \boldsymbol{\omega} \times \mathbf{r} + \mathbf{v}_{rel}\right) \tag{48}$$

Despite the fact that the evaluation of Eqs. (46) can be easily performed on structured discretizations by using finite difference approximations, a more general approach is needed for arbitrary body discretizations. In this work the derivatives are evaluated at each panel using the value of the doublet strength at the panel's corner points i. These are obtained by

$$\mu^i = \frac{\sum\limits_{j=1,ns_i} A_j \mu_j}{\sum\limits_{j=1,ns_i} A_j} \tag{49}$$

where A_j and μ_j are the surface area and doublet strength of a panel j respectively, and the summation is performed over the ns_i panels surrounding the corner point i. Once the doublet strengths at the panel's corner points are determined, the derivatives (46) are evaluated (in panel coordinates) by using a standard finite element approximation.

2.2.3 Suspension lines and internal flow treatment

In addition to the aerodynamic loads on the parachute canopy, wind loads are applied to the suspension and control lines. These loads are computed in a simplified manner by considering the cords as long cylinders exposed to the wind. Thus, experimental drag coefficients can be applied and the aerodynamic force is computed taking into account the magnitude of the local dynamic pressure and the direction of the total velocity vector acting on the cable elements.

The flow inside the parachute cells is not taken into account by the code. Therefore a constant stagnation pressure is applied inside the canopy to keep it pressurized. Note that the air intakes of the canopy must be panelized in order to obtain a closed shape (as required by the aerodynamic model employed). However, no aerodynamic loads are computed or applied on these panels. Furthermore, to prevent the intake panels from interfering with the structural behaviour of the canopy they are made extremely flexible. They are assigned a very small relative thickness and an extremely low Young's modulus. Their load bearing capacity is thus negligible compared with the rest of canopy panels.

2.3 Coupling the aerodynamic and structural modules

A simple coupling scheme between the aerodynamic (A) and structural (S) solvers is adopted in the parachute simulation code. Transfer of data is straightforward as the A & S models share the same mesh. The aerodynamic mesh may contain quadrilateral and/or triangular panels. When a quadrilateral element is passed to the structural solver it is internally split into a pair of triangles in order to carry out the analysis. As the stability limit of the explicit structural solver is small, several structural iterations are performed for each aerodynamic time step. Due to the fact that the aerodynamic loads are not updated at every step the high order (i.e. high frequency) response of the structure is not captured. For normal design tasks this is not a serious limitation as the high-frequency modes are of low amplitude and affect only small parts of the structure. Parachute designers are usually interested in the overall response where the effect of the low frequency modes is dominant. These are well resolved using the simple coupling scheme adopted. In those cases where only a steady state solution is sought, convergence can be accelerated by using an under-relaxation technique when transferring aerodynamic loads to the structure.

3. CODE VALIDATION

In order to assess the accuracy of the structural and aerodynamic solvers some example problems for which reference solutions are available are presented.

3.1 Structural solver validation cases

The most challenging aspects of the structural response are the large displacements involved as well as the asymmetric behaviour due to wrinkling. Two benchmarks illustrating these capabilities are presented. First, the deformed shape of a cable (and ribbon) subject to its own weight is computed. The stiffness of the cable is large enough to neglect the effect of stretching. The schematic undeformed (dashed line) and final configurations (solid line) are shown in Fig. 7.
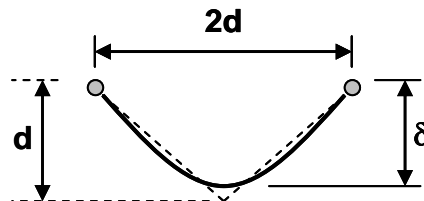
Figure 7. Catenary problem definition.

From elementary mechanics it is known that the deformed shape of the cable is a catenary. For the particular set of boundary conditions chosen the height of the catenary is $\delta = 0,895d$. The cable has been discretized with 20 linear elements. In order to check also the behaviour of the membrane formulation a strip made of triangular elements has been suspended the same way as the cable. The strip is modelled with a mesh of 20x4 triangles. The values predicted by the structural solver are given in Table 1. The agreement between the analytical result and the numerical results is excellent. The deformed mesh is shown in Fig. 8.

	Cable elements	Membrane elements
δ/d	**0,896**	**0,897**[1]

Table 1 Computed geometry for the catenary problem.
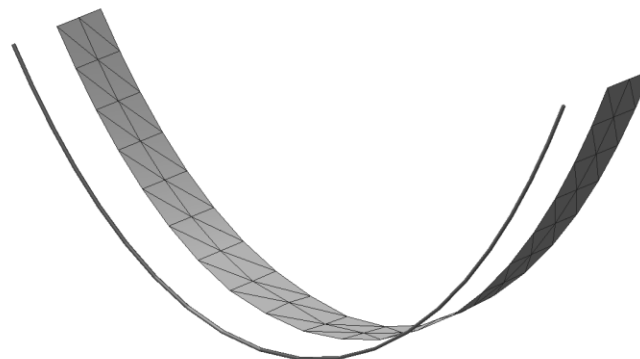
Figure 8. Deformed mesh for the catenary problem.

---

[1] Value for the triangular elements is an average. Due to the constraints imposed by the discretisation the deformed shape is not perfectly cylindrical.

The airbag inflation test is a suitable test check of the wrinkling capability. This benchmark computes the vertical displacement at the centre of an initially flat square airbag of side length 840mm. An internal pressure of 5kPa is applied. The deformed configuration is strongly affected by the no-compression condition on the fabric, so this is a very popular benchmark for wrinkling models. The textile properties are:

$$E = 588 MPa \; ; \; t = 0,6mm \; ; \; \nu = 0,4 \tag{50}$$

A mesh composed of 16x16 squares is used for each side of the airbag. Each square has then been divided into 4 equal triangles in order to eliminate mesh orientation effects. The total number of triangular elements is therefore 2048. The next table shows the comparison of the result from the parachute simulation tool (named PARA_STR in the table) with several sources [11-13]. The differences are negligible. The deformed configuration is shown in Fig. 9.

	Contri	Ziegler	Hornig	PARA_STR
Deflection (mm)	217,0	216,0	216,3	216,2

Table 2 Central displacement of the airbag (mm).
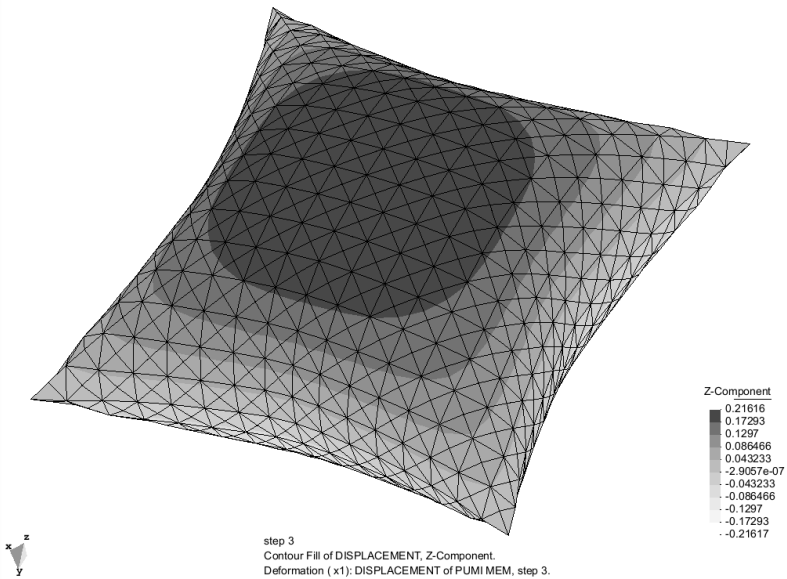
Figure 9. Deformed shape for the airbag inflation benchmark.

3.2 Flow solver test cases

Two unsteady test cases are presented in this section in order to assess the performance of the aerodynamic solver. The first example involves the impulsive movement of a rectangular wing having a uniform NACA 0012 section along the span and an aspect ratio A = 4. The discretization consists of 25 quadrilateral panels in the chordwise direction and another 35 along the span (1750 panels). An initial non-dimensional time increment

$\Delta t^* = U_\infty \Delta t / c = 0.025$ and an angle of attack $\alpha = 5^\circ$ are adopted. Figure 10 depicts the unsteady wake developed behind the wing, as it moves in the stationary air. The wing starting vortex can be observed.
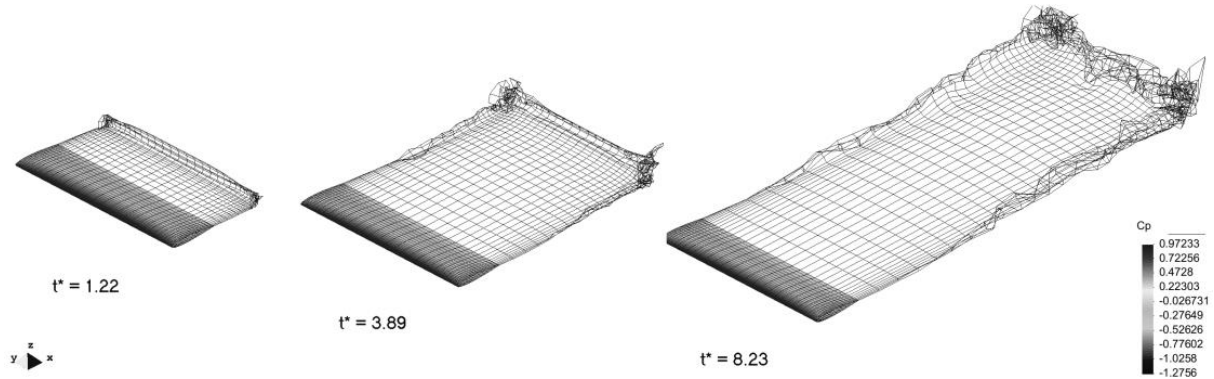

Figure 10. Wing and wake snapshots at different instant times after the wing is suddenly set into motion. Cp results are displayed (A=4 and α=5°).

The unsteady lift coefficient of the wing (C_L) is computed and the results are plotted in Figure 11 together with some discrete points taken from [8]. A good agreement can be observed between the results.
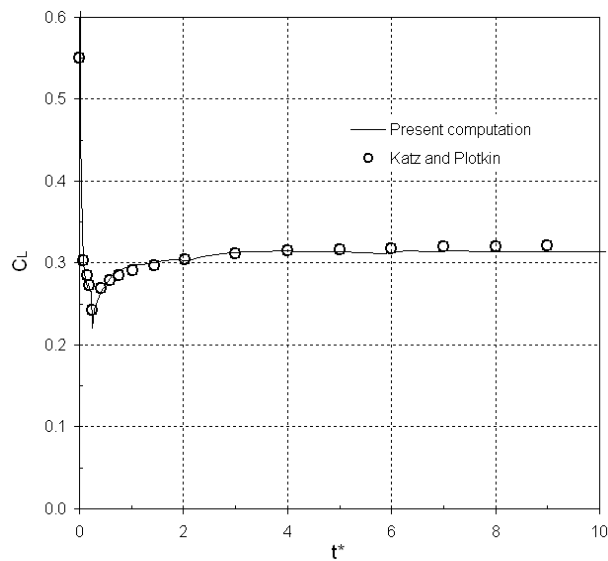
Figure 11. Unsteady lift coefficient for a rectangular wing suddenly set into motion (A=4 and α=5°).

In the second example, the two-bladed rotor studied experimentally in [14] is solved. In order to minimize the compressibility effects that may affect the comparisons, a rotor speed $\Omega_z = 650\,\text{rpm}\,(M_{tip} \approx 0.225)$ is selected according to the lowest angular velocity tested in the study taken as reference. The rotor geometry is discretized with a structured mesh of 4000 quadrilateral panels (40 along the span and 25 in the chordwise direction). Figure 12 presents

the Cp distribution computed for a collective pitch angle $\theta_c = 8°$ after the rotor has completed several turns.

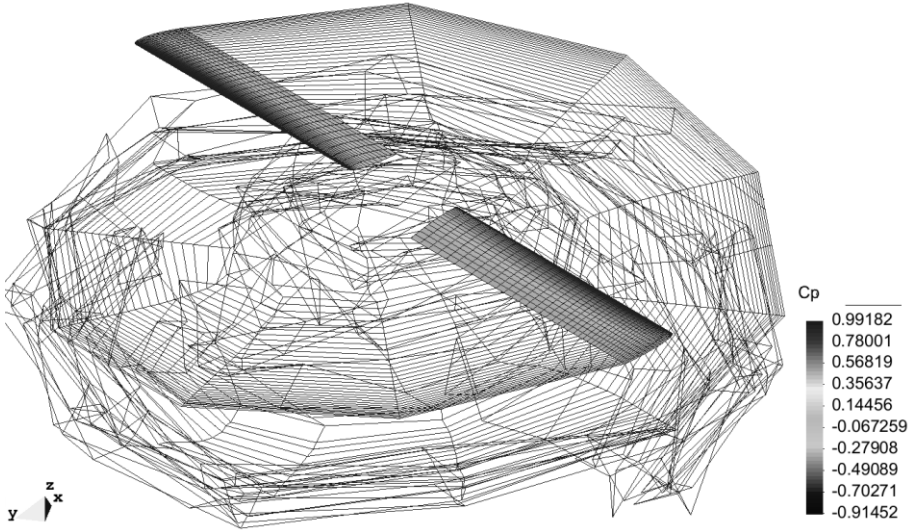**Figure 12**. Cp distribution computed over blades for a collective pitch angle $\theta_c = 8°$.

Cp distributions are computed on different sections along the blade for collective pitch angles $\theta_c = 5°$ and $8°$ and the results are compared with experimental measurements [14] in Figure 13. A good correlation can be observed between numerical and experimental results, although the wake model adopted could be further improved (wake movements are limited to avoid body and wake panels intersections).
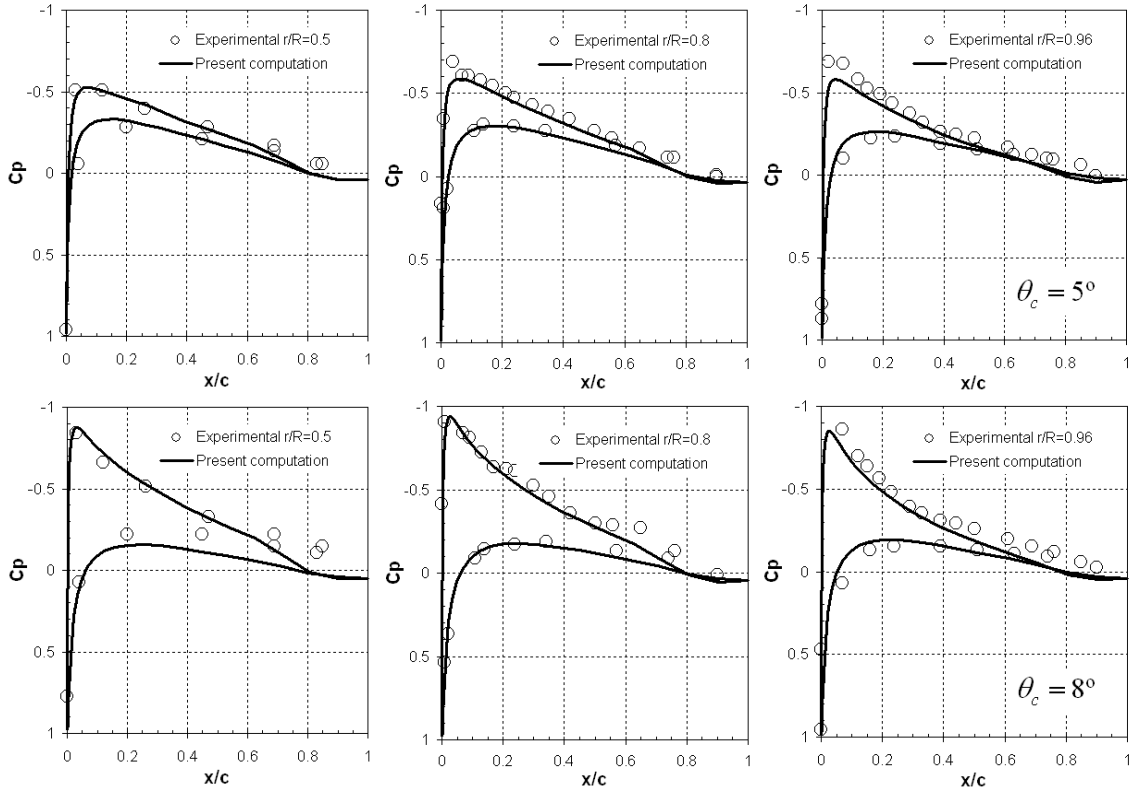
Figure 13. Comparisons of numerical and experimental Cp distributions at different sections along a blade.

4. EXAMPLES OF APPLICATION TO PARACHUTES

Three test cases are presented in this section to demonstrate the potential of the numerical tool to analyze real parachute problems.

4.1 Stationary analysis of a large ram-air parachute

Steady aerodynamic characteristics of a large ram-air parachute are investigated in this example and the results are compared with experimental measurements given in [15]. The model is a high glide-performance parachute aimed at delivering very heavy payloads designed and manufactured by CIMSA in the framework of the FASTWing Project [16]. The model canopy discretization consists of an unstructured distribution of 11760 triangular elements and 11912 cable elements model the suspension and control lines as well as the reinforcement tapes integrated into the canopy. The freestream velocity is set to 23 m/s and the simulation is initialized with a partially inflated parachute configuration. The movement of the suspension line's confluence points is restricted to follow the experimental setup. To obtain a faster convergence to the equilibrium position of the parachute, some degree of under-relaxation is employed when transferring the aerodynamic loads to the structure. Initial and equilibrium parachute configurations are shown in Figure 14.
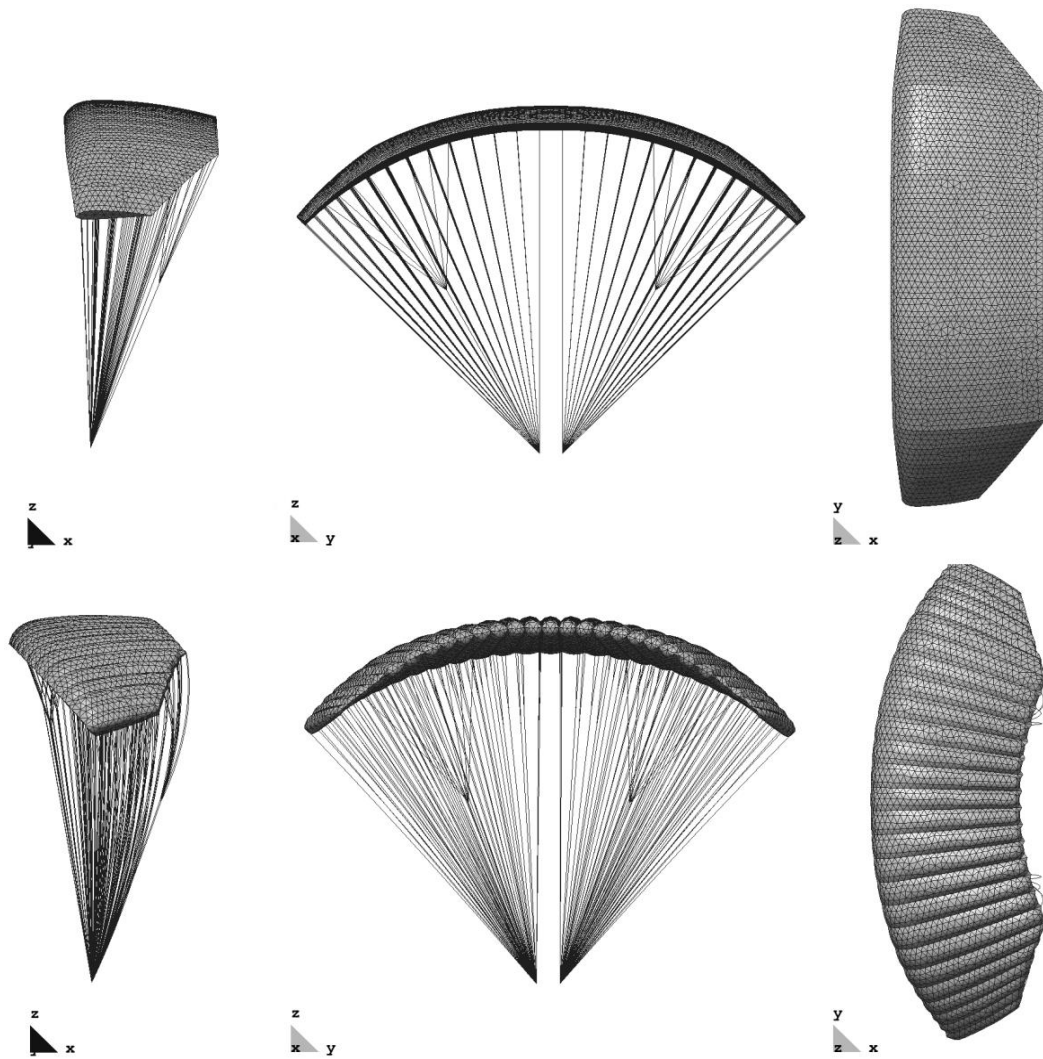
Figure 14. Three views of the initial (top) and computed (bottom) equilibrium configurations.

The time history of force and moment coefficients is displayed in Figure 15, where the moment coefficients are computed about a point located between the suspension line's confluence points. Note that the moments plotted include only the contribution due to the canopy, if the contribution of the drag from the suspension lines were included the total value would be zero. Bear in mind also that the transient behaviour lacks real physical meaning as under-relaxation has been employed to accelerate the problem convergence to the steady state solution.
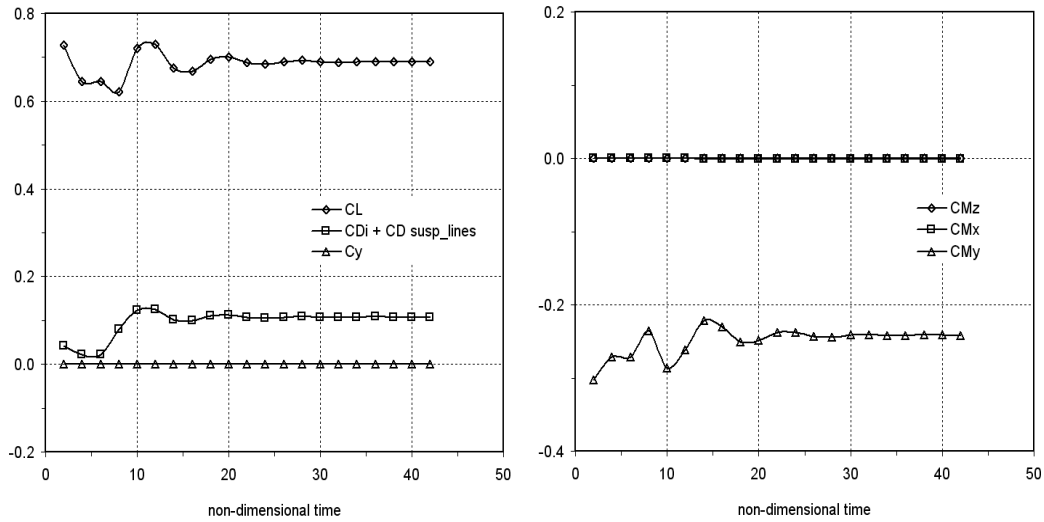
Figure 15. Computed time history of forces and moments coefficients.

Considering the equilibrium lift and drag coefficients displayed in Figure 15, a numerical angle of descent $\Gamma = C_D / C_L \approx 10^\circ$ can be estimated. Next, Figure 16 shows Cp distribution computed over the parachute for the equilibrium condition.
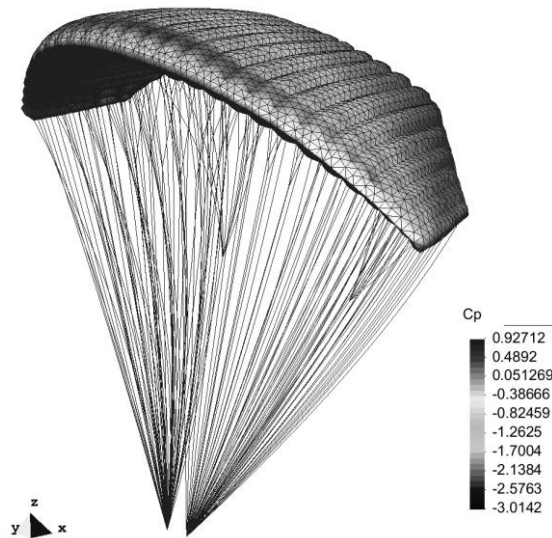

Figure 16. Parachute pressure coefficient, $\Gamma \approx -10^\circ$.

Experimental measurements report stationary lift and drag coefficients of $C_L = 0.577$ and $C_D = 0.179$, which yield a descent angle $\Gamma \approx 17^\circ$. The numerical model predicts a higher efficiency (a smaller glide path angle) but this was expected due to the characteristics of the model. The difference is partly due to the fact that the potential flow model overestimates lift as the entire flow around the canopy is considered to be attached. The drag coefficient is on the other underestimated as skin friction drag and shape drag on the canopy were not

25

accounted for in this simulation. In case of need it is possible to account for viscous effects using boundary layer theory or semi-empirical corrections. However, as pointed out in the introduction, extremely important information can be obtained from the uncorrected results because they provide a good estimation of the flight shape of the canopy and the stresses on the different components.

4.2 Parachute manoeuvre analysis

A left-turn manoeuvre of a small CIMSA parachute-payload system subject to gravity loads is studied in this example. The canopy discretization consists of an unstructured distribution of 9548 triangular elements and 3077 cable elements model the suspension lines and the canopy reinforcements. The payload is 100 kg and the parachute is released with North heading at a velocity of 12 m/s. The simulation starts with a partially inflated parachute configuration and, once steady descent flight is achieved, the manoeuvre is initiated by applying a 0.5 m downward deflection of the left brake line. After 5 seconds, the brake line is released and the parachute recovers a straight down descent flight. The trajectory described by the payload center of gravity during the manoeuvre is displayed in Figure 17. Some snapshots of the parachute-payload system taken at different times during the simulation are shown in Figure 18.
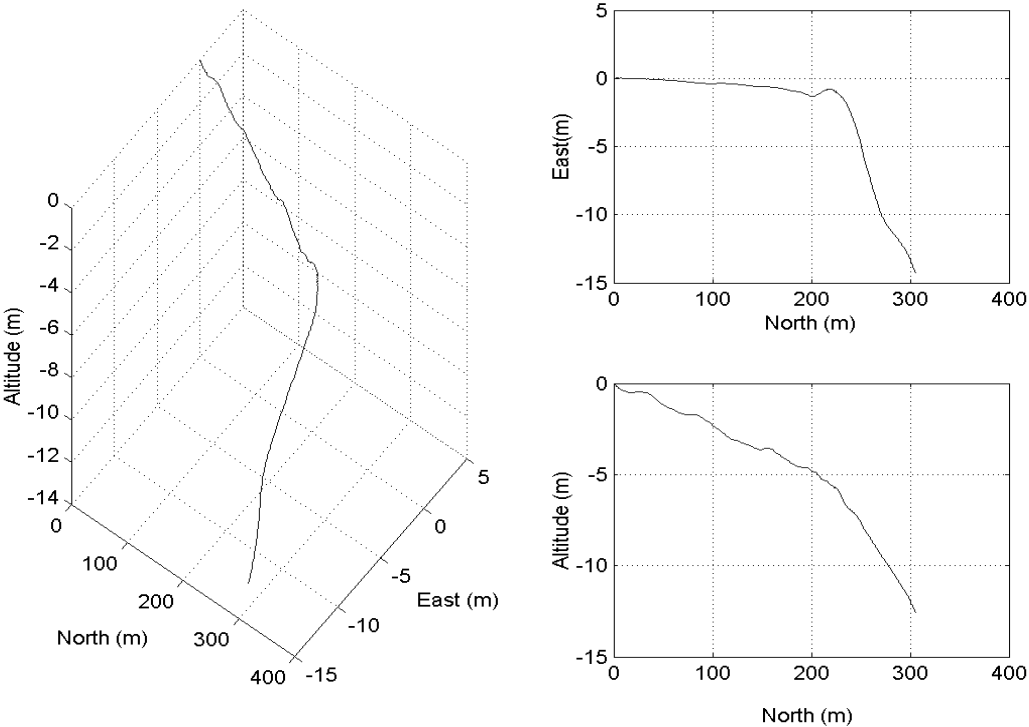

Figure 17. Payload centre of mass computed trajectory.

In spite of the fact that no quantitative experimental data is available for this test case, the numerical results match those observed in real behaviour of ram-air parachutes performing the same manoeuvre. This demonstrates the capability of the present methodology to provide not only aerodynamic and structural data for design but also for performance and trajectory analyses.
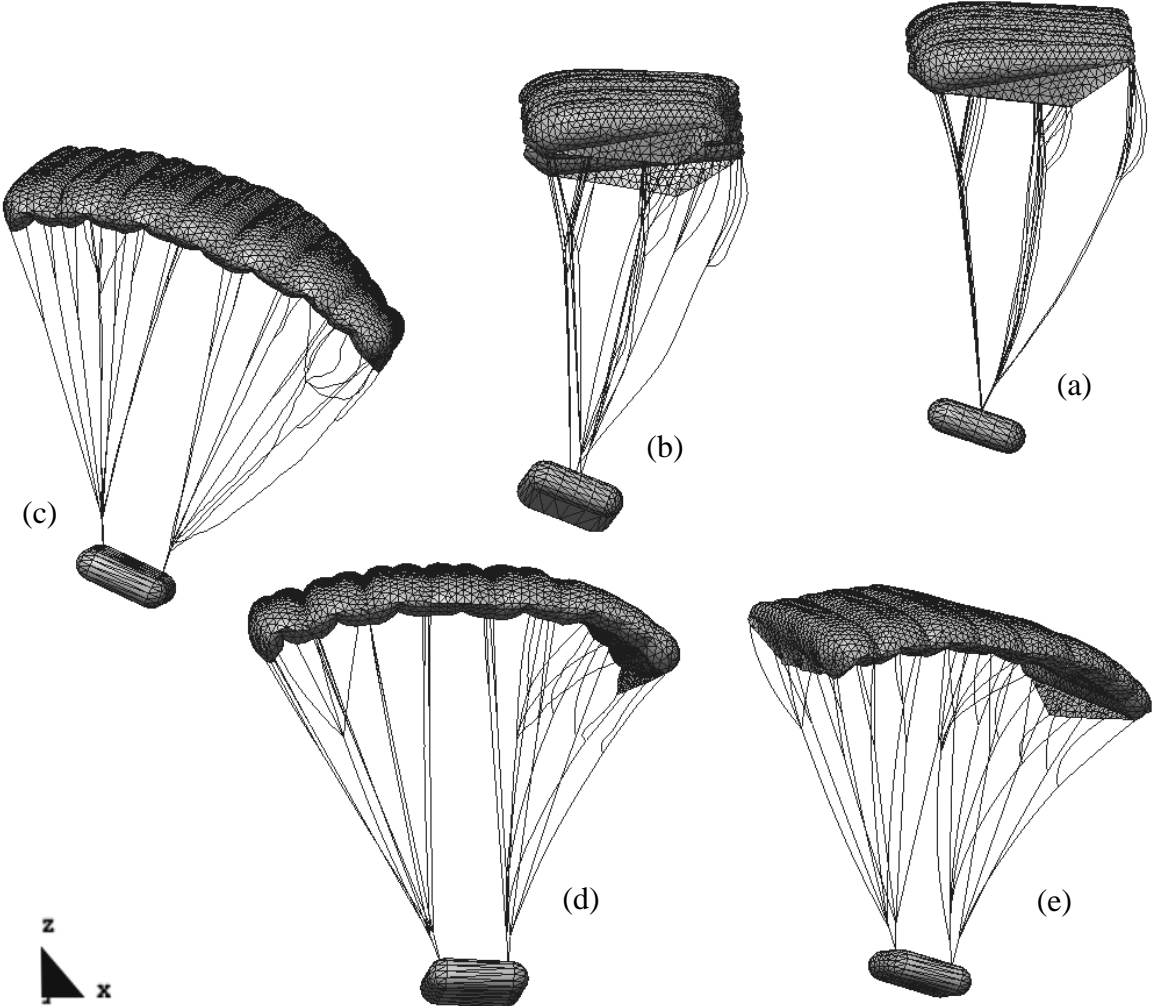

Figure 18. Several snapshots of the parachute-payload configuration at different stages of the manoeuvre simulation: (a) 3.564 secs, (b) 15.58 secs, (c) 19.05 secs, (d) 19.88 secs., (e) 23.17 secs.

4.3 Inflation process of a conventional parachute

This is a simple inflation test aimed at exploring the capabilities of the computational code to simulate parachute deployment and inflation. The model proposed for the aerodynamic loads is quite simple. The parachute is initially deployed by applying a force at the canopy apex in the direction of the incident wind. The inflation stage, which begins after line and canopy stretching, occurs due to a variable pressure force applied on the canopy accounting for

relative wind direction and velocity. In this way, the maximum pressure force corresponds to the fluid stagnation condition and the value is reduced according to the orientation of the elements in relation to the incident wind. The parachute is discretized with an unstructured distribution of 3390 triangular elements and 2040 cable elements modeling the suspension lines and the fabric reinforcements. The canopy has a surface area $S_0 = 222.25\,m^2$ and, once deployed, its projected cross-section becomes $S_p \approx 0.44 S_0$. The freestream velocity is set to $V_\infty = 28.5\,m/s$. Some snapshots of the parachute at different times during the inflation process are presented in Figure 19.
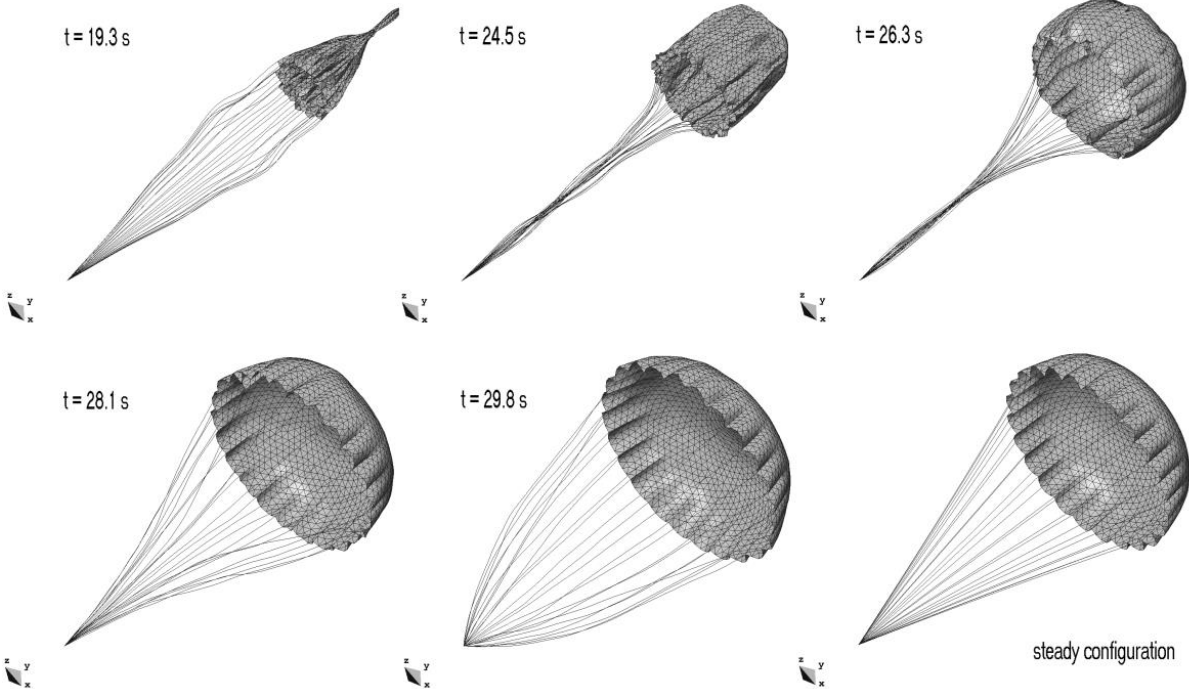

Figure 19. Parachute views at different instant times during the inflation phase.

The reaction force computed at the confluence point during the inflation process is shown in Figure 20. A satisfactory agreement with experimental results reported in [17] for similar configurations has been observed.
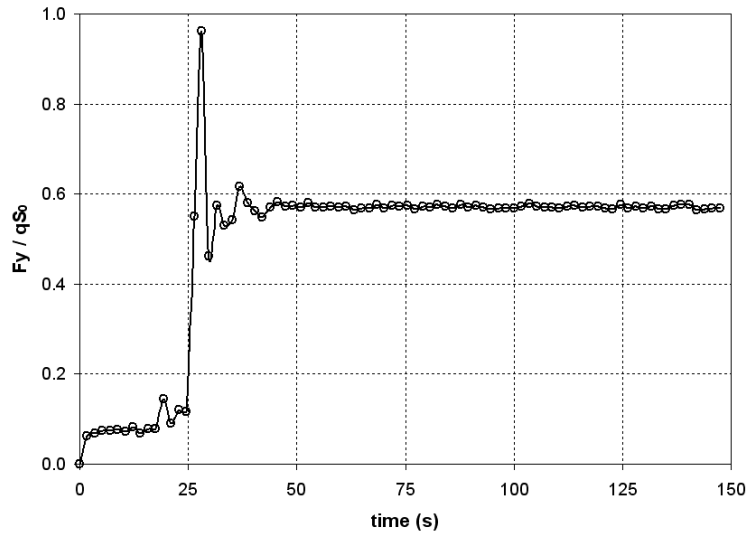
Figure 20. Evolution of the parachute opening force.

Future developments in parachute deployment and inflation simulation are to be focused on evaluating the feasibility of more-accurate semi-empirical models such as filling distance, kinetics and momentum methods. These inflation theories can be implemented with a low computational cost and have been applied to a wide range of problems with satisfactory results; see [18] for a review.

5. CONCLUSIONS

The important role parachutes play in many civil, humanitarian and military applications calls for new and improved computational tools aimed at tackling the current lack of software applications in the field. A new development from CIMNE in this direction has been presented. The simulation package contains a coupled fluid-structural solver tailored for the unsteady simulation of ram-air type parachutes. The capabilities of both the dynamic explicit structural code and the unsteady potential flow solver have been successfully validated through relevant benchmark cases. The coupled solution approach has been successfully applied to a variety of problems encountered during parachute design activities. The solution strategy is robust and the code shows a notable efficiency, being able to treat complex systems with only limited computational resources (all the examples presented have been run on mid-range desktop computers). As it has been highlighted throughout this work, the challenges involved in the simulation of parachutes are not minor. However, the numerical results obtained to date encourage us to further advance in the development of the software, as it addresses an important need of the parachute industry for which there is currently no established solution.

ACKNOWLEDGEMENTS

REFERENCES

[1]   Drukker, J. and Roddeman, D. G. The wrinkling of thin membranes: Part 1 - Theory. *Journal of Applied Mechanics,* 54:884-887, 1987.

[2]   Drukker, J. and Roddeman, D. G. The wrinkling of thin membranes: Part 2 - Numerical analysis. *Journal of Applied Mechanics,* 54:888-892, 1987.

[3]   Guerra, A. Development and validation of a numerical code for analyzing parachutes. Undergraduated thesis presented at the Scola Tecnica Superior d'Enginyers Industrial i Aeronàutica de Terrassa, Technical University of Catalonia (in Spanish). 2009.

[4]   Belytschko, T., Liu, W.K., and Moran, B. Nonlinear finite elements for continua and structures. John Wiley & Sons, 2000.

[5]   Zienkiewicz, O.C., Taylor, R.L. and Zhu, J.Z. *The finite element method*: *Its basis and fundamentals*. Vol 1, Butterworth-Heinemann, 2005.

[6]   Taylor, R.L. Finite element analysis of membrane structures. Publication PI-203, CIMNE, 2001.

[7]   Rossi, R. A finite element formulation for 3D membrane structures including a wrinkling modified material model. Publication PI-226,CIMNE, 2003.

[8]   Katz, J. and Plotkin, A. Low-Speed aerodynamics. From wing theory to panel methods., McGraw-Hill, 1991.

[9]   Maskew, B. Program VSAERO theory document. A computer program for calculating nonlinear aerodynamic characteristics of arbitrary configurations. *NASA Report 4023,* 1987.

[10]   Ashby, D. L. Potential flow theory and operation guide for the panel code PMARC_14. *NASA TM-1999-209582,* 1999.

[11]   Contri, P. and Schrefler, B. A. A geometrically nonlinear finite element analysis of wrinkled membrane surfaces by a no-compression material model. *Communications in applied numerical methods,* 4: 5-15, 1988.

[12]   Ziegler, R., Wagner, W., and Bletzinger, K. A multisurface concept for the finite element analysis of wrinkled membranes. *Proceedings of the 4th International colloquium on computation of shell & spatial structures, IASS – IACM,* 2000.

[13]   Hornig, J. Analyse der Faltenbildung in Membranen aus unterschiedlichen Material. *PhD thesis, Technischen Universität Berlin,* 2004.

[14]   Caradonna, F. X. and Tung, C. Experimental and analytical studies of a model helicopter rotor in hover. *NASA Technical Memorandum NASA-TM-81232,* 1981.

[15]   Hollestelle, P. The FASTWing Project: Wind tunnel test - Realisation and results. *18th AIAA Aerodynamic Decelerator Systems Technology Conference and Seminar. AIAA paper 2005-1641,* 2005.

[16]   Benolol, S. and Zapirain, F. The fastwing project, parafoil development and manufacturing. *18th AIAA Aerodynamic Decelerator Systems Technology Conference and Seminar. AIAA paper* 2005-1639, 2005.

[17]   Scher, S. H. and Young, I. G. Drag coeficcients for partially inflated flat circular parachutes. *NASA Technical Note D-6423,* 1971.

[18]   Cockrell, D. J. The aerodynamics of parachutes. *AGARDograph Nº 295. AGARD-AG-295,* 1987.

[19]   CIMSA Ingeniería y Sistemas Web page: http://www.cimsa.com/ (access date February 8th 2011).

[20]   Takizawa, K., Bazilevs, Y. and Tezduyar, T.E., Space-time and ALE-VMS techniques for patient-specic cardiovascular fluid-structure interaction modeling. *Arch. Comput. Methods Eng.*, 4:341-379, 2012.